

Article

# Elastic Scattering of Slow Electrons by Noble Gases—The Effective Range Theory and the Rigid Sphere Model

Kamil Fedus 

Institute of Physics, Faculty of Physics, Astronomy and Informatics, Nicolaus Copernicus University, Grudziadzka 5/7, 87-100 Torun, Poland; kamil@fizyka.umk.pl

**Abstract:** We report on an extensive semi-empirical analysis of scattering cross-sections for electron elastic collision with noble gases via the Markov Chain Monte Carlo-Modified Effective Range Theory (MCMC–MERT). In this approach, the contribution of the long-range polarization potential ( $\sim r^{-4}$ ) to the scattering phase shifts is precisely expressed, while the effect of the complex short-range interaction is modeled by simple quadratic expression (the so-called effective range expansion with several adjustable parameters). Additionally, we test a simple potential model of a rigid sphere combined with  $r^{-4}$  interaction. Both models, the MERT and the rigid sphere are based on the analytical properties of Mathieu functions, i.e., the solutions of radial Schrödinger equation with pure polarization potential. However, in contrast to MERT, the rigid sphere model depends entirely upon one adjustable parameter—the radius of a hard-core. The model’s validity is assessed by a comparative study against numerous experimental cross-sections and theoretical phase shifts. We show that this simple approach can successfully describe the electron elastic collisions with helium and neon for energies below 1 eV. The purpose of the present analysis is to give insight into the relations between the parameters of both models (that translate into the cross-sections in the very low energy range) and some “macroscopic” features of atoms such as the polarizability and atomic “radii”.

**Keywords:** electron elastic scattering; noble gases; scattering cross-sections



**Citation:** Fedus, K. Elastic Scattering of Slow Electrons by Noble Gases—The Effective Range Theory and the Rigid Sphere Model. *Atoms* **2021**, *9*, 91. <https://doi.org/10.3390/atoms9040091>

Academic Editors: Michael Brunger and David D. Reid

Received: 17 August 2021

Accepted: 27 October 2021

Published: 29 October 2021

**Publisher’s Note:** MDPI stays neutral with regard to jurisdictional claims in published maps and institutional affiliations.



**Copyright:** © 2021 by the authors. Licensee MDPI, Basel, Switzerland. This article is an open access article distributed under the terms and conditions of the Creative Commons Attribution (CC BY) license (<https://creativecommons.org/licenses/by/4.0/>).

## 1. Introduction

Although great attention was devoted to electron collisions with atoms of noble gases over the years [1], scattering in a very low-energy range is still challenging both experimentally and theoretically. On the one hand, experiments at very low energies are scarce and burdened with high uncertainties since hard-to-reach energy and angular resolutions are required to carry out trustworthy measurements [2]. On the other hand, the theoretical description of complex (many-body) short-range effects in the electron–atom collision reached a high level of fidelity (see for example [3,4]), but numerical calculations become more and more computationally expensive and time-consuming with lowering electron energy. The most advanced contemporary theories involve such large basis sets and complicated equations that they are not easily applied to each specific target for which data are needed urgently. Therefore, a great value in understanding angular and energy variations of low-energy collisions can be brought by semi-empirical models, which give some insight into the relations between cross-sections and some “macroscopic” (i.e., measurable in other phenomena) features of the targets, like their polarizability and/or atomic “radii”. Surprisingly, the very low-energy range is important for plasma modeling: say, in argon, which is the main component of “gas-discharge lamps”, the mean temperature of electrons is 0.3 eV, i.e., the energy of the Ramsauer–Townsend minimum [5]. Noble gases are used also as additives in swarm experiments, to derive the very-low energy cross sections for molecules with other possible processes, like the vibrational excitations (CH<sub>4</sub>, C<sub>2</sub>H<sub>2</sub> [6,7]).

The effective range theory (ERT) is one of the most popular semi-empirical ways to describe slow-electron collisions with atoms. Originally, ERT has been introduced as a tool in the analysis and interpretation of low-energy neutron–proton scattering [8,9]. The theory expresses the *s*-wave scattering phase shift as a series of the projectile (neutron) momentum *k*. The series contains two adjustable parameters:  $A_0$ —the scattering length and  $R_0$ —the effective range of the interaction. O’Malley et al. [10] modified the ERT to show that a similar expression could be used to describe the scattering of a charged particle (such as electron and positron) by neutral atoms and simple non-polar molecules, i.e., in the presence of the long-range polarization potential ( $\sim r^{-4}$ ). Later similar energy series expansions to that for *s*-wave phase-shift were introduced for higher partial waves (*p* and *d* waves) [11]. Due to its simplicity, the Modified Effective Range Theory (MERT) has gained considerable popularity. It has been frequently used to extrapolate measured cross-sections to the zero-energy [12–17]. Moreover, it is also used as a support for complex multi-body calculations to determine the scattering length, see, for example [18,19].

Buckman and Mitroy [20] showed that the applicability of the original MERT is limited to very low energies (<1 eV) for noble gases. At such low energies, the experimental data to be extrapolated are scarce and characterized by relatively large uncertainties. The variety of experimental technique reflects in different possible systematic uncertainties. In case of integral (total) cross sections (ICS) these may be errors in pressure determination (due to the gas outflow from the scattering cell), angular resolution errors (due to the finite dimensions of detectors) and shift in energy determination (due to extremely fast timing of the signal in time-of-flight experiments). In the case of differential cross sections (DCS)—additionally, the impossibility of measuring small (below 10°) and large (above some 130°) scattering angles plays an important role. The contribution of all these errors to experimental data makes the MERT analysis less reliable. Idziaszek and Karwasz [21] proposed an alternative approach to the MERT series: phase shifts were obtained solving the Schrödinger equation with long-range polarization potential analytically using Mathieu functions, and the effective-range expansion was introduced only for the short-range part of the interaction potential. We showed [22–25] that such an approach allows expanding MERT applicability to much higher energies, where more accurate data are available. It is true for both positrons and electrons. The most significant advantage of the method is its simplicity—just a few parameters are used to describe the effect of complex, many-body interaction during the electron/positron collisions with atoms and molecules. Moreover, a new approach to MERT can be used to correct *ex posteriori* the experimental errors, as shown in [16]. Furthermore, understanding the physics behind the MERT parameters can help to provide more valuable data for an inverse scattering theory approach [26]. This approach aims to reconstruct the scattering potential from the experimental cross-sections, and MERT can potentially be a part of the inversion procedure.

In [27], we showed that an even simpler semi-empirical model than MERT could describe very low-energy positron (antielectron) interaction with noble gases, namely the rigid sphere approach. In this model, the interaction is described as a combination of an infinite wall (hard-sphere) and the long-range polarization potential ( $\sim r^{-4}$ ). Consequently, one needs just one parameter (“the atomic radii”) to describe cross-sections at energies much below 1 eV. So far, this simple model has not been tested thoroughly for electron scattering by single atoms.

The goal of the present work is twofold. Firstly, we carry out an extensive (statistical) MERT analysis of a vast amount of datasets for electron collision with noble gases to study the systematics of parameters appearing in the effective-range expansion of the short-range potential. Using Monte Carlo methods, we provide confidence ranges for MERT parameters that are crucial for accurate predictions of cross-sections at low energies. At the same time, we examine the convergence of various available experimental data within the applied model. Secondly, we verify the applicability of the rigid sphere model to the low-energy electron scattering by noble gases. The paper is organized as follows: in Section 2, the principles of MERT and the rigid sphere model are briefly described.

In Section 3, the results of both models are presented and discussed. The paper concludes with a summary in Section 4.

## 2. Theoretical Models

### 2.1. Modified Effective Range Theory

The relative motion of a light electrically charged point particle and closed-shell atom is described by the following radial Schrödinger equation (within a partial-wave formalism in atomic units):

$$\left[ \frac{d^2}{dr^2} - \frac{l(l+1)}{r^2} + \left( \frac{e^2\mu}{\hbar^2} \right) \frac{\alpha}{r^4} + V_s(r) + k^2 \right] \Psi_l(r) = 0, \tag{1}$$

where  $l$  is the angular momentum quantum number,  $k$  is the wavenumber,  $\alpha$  is the dipole polarizability, and  $V_s(r)$  is the short-range potential. Note that the atomic units are employed throughout this paper. In particular, the electron mass ( $m_e$ ), the Planck constant ( $\hbar$ ) and the elementary charge ( $e$ ) are equal to unity. Consequently, the reduced mass of the electron–atom system ( $\mu$ ) can be also approximated to one.

Since  $V_s(r)$  can be neglected at large  $r$ , O'Malley et al. [10] proposed to include its contribution in appropriate boundary conditions subjected to analytical solutions of the Schrödinger equation with pure long-range polarization potential ( $\sim r^{-4}$ ):

$$\left[ \frac{d^2}{dr^2} - \frac{l(l+1)}{r^2} + \left( \frac{e^2\mu}{\hbar^2} \right) \frac{\alpha}{r^4} + k^2 \right] \Phi_l(r) = 0. \tag{2}$$

The latter equation is identical with Mathieu's modified differential equation; hence  $\Phi_l(r)$  can be expressed in terms of Mathieu functions, whose behavior at small and large distances  $r$  is determined by the standard boundary conditions (according to the quantum scattering theory) imposed on the scattering wavefunction:

$$\Phi_l(r) \stackrel{r \rightarrow 0}{\sim} r \sin\left(\frac{\sqrt{\alpha}}{r} + \gamma_l\right) \text{ and } \Phi_l(r) \stackrel{r \rightarrow \infty}{\sim} \sin(kr - l\frac{\pi}{2} + \eta_l) \tag{3}$$

where  $\gamma_l$  is a parameter determined by the short-range part of the interaction potential, while  $\eta_l$  is the scattering phase shift.

The boundary conditions provide the following expression for the scattering phase shift:

$$\tan \eta_l = \frac{m_l^2 - \tan^2 \delta_l + B_l \tan \delta_l (m_l^2 - 1)}{\tan \delta_l (1 - m_l^2) + B_l (1 - m_l^2 \tan^2 \delta_l)}, \tag{4}$$

where  $B_l = \tan(\gamma_l + l\pi/2)$  and  $\delta_l = \frac{\pi}{2}(v_l - l - \frac{1}{2})$ . Here  $m_l$  and  $v_l$  denote the energy-dependent parameters which can be determined numerically from properties of the Mathieu functions (see the numerical procedures described in [21,22]).

Integral elastic ( $\sigma_{IE}$ ), momentum transfer ( $\sigma_{MT}$ ), and differential elastic ( $d\sigma/d\omega$ ) cross-sections (all measured experimentally) are calculated using the standard partial wave expansions:

$$\sigma_{IE} = \frac{4\pi}{k^2} \sum_{l=0}^{\infty} (2l+1) \sin^2 \eta_l(k) \tag{5}$$

$$\sigma_{MT} = \frac{4\pi}{k^2} \sum_{l=0}^{\infty} (l+1) \sin^2 [\eta_l(k) - \eta_{l+1}(k)] \tag{6}$$

$$\frac{d\sigma}{d\omega} = \frac{1}{k^2} \left| \sum_{l=0}^{\infty} (2l+1) \exp i\eta_l \sin \eta_l(k) P_l(\cos \theta) \right|^2 \tag{7}$$

where  $\theta$  is the scattering angle and  $P_l(x)$  are the Legendre polynomials.

O'Malley et al. [10] showed that energy dependence of parameter  $B_l(k)$ , related to the unknown short-range potential, has the following general form:

$$B_l(k) = b_l(0) + \frac{1}{2} \sqrt{\alpha e^2 \mu / \hbar^2} \rho_l(0, k) k^2. \tag{8}$$

where  $b_l(0)$  is the zero-energy contribution and

$$\rho_l(0, k) = \int_0^\infty \Phi_l(0, r) \Phi_l(k, r) - \Psi_l(0, r) \Psi_l(k, r) dr. \tag{9}$$

Thus far all equations are exact. O'Malley et al. [10] proposed to approximate the latter parameter by the energy-independent value at zero-energy. Then  $B_l(k)$  takes a form:

$$B_l(k) \approx b_l(0) + \frac{1}{2} \sqrt{\alpha e^2 \mu / \hbar^2} R_l k^2, \tag{10}$$

where  $R_l = \rho_l(0, 0)$ . Equation (10) is similar to the effective range expansion of the scattering phase-shift in absence of the long-range potentials used to describe neutron–proton collisions [8,9]. Hence, in analogy to the original effective-range theory, we can call  $R_l$  as the “effective-range”, though the physical meaning of this parameter is rather different. Since the error is of the order  $k^4$ , it is expected that the approximation is valid at low energies. We have already shown [21,22] that  $\rho_l(0, k)$  changes rather slowly with increasing energy since MERT (using approximation (10)) is able to describe the scattering cross-sections almost up to the energy thresholds for the first inelastic processes.

In the zero energy limit both integral elastic (Equation (5)) and momentum transfer cross-sections (Equation (6)) can be expressed by the  $s$ -wave scattering length ( $A_0$ ):

$$\sigma_{IE}(k) \approx \sigma_{MT}(k) = 4\pi A_0^2, \text{ for } k \rightarrow 0. \tag{11}$$

The  $s$ -wave scattering length can be expressed in terms of  $b_0$  as  $A_0 = -\sqrt{\alpha e^2 \mu / \hbar^2} / b_0$ .

At low energies, the leading contributions come mainly from the first two or three partial waves ( $l = 0, 1, 2$ ) while the contributions of higher partial waves are small and they are not modified by the short-range forces due to very high centrifugal barriers associated with large  $l$  numbers. Therefore the scattering phase-shifts experienced by higher partial waves can be described by the relations provided by Ali and Fraser [28]:

$$\tan \eta_l(k) = \alpha a_l k^2 + (\alpha^2 b_l + \beta c_l) k^4, \text{ for large } l, \tag{12}$$

where

$$a_l = \frac{\pi}{(2l + 3)(2l + 1)(2l - 1)}, \tag{13}$$

$$b_l = \frac{\pi [15(2l + 1)^4 - 140(2l + 1)^2 + 128]}{[(2l + 3)(2l + 1)(2l - 1)]^3 (2l + 5)(2l - 3)}, \tag{14}$$

$$c_l = \frac{3\pi}{(2l + 5)(2l + 3)(2l + 1)(2l - 1)(2l - 3)}. \tag{15}$$

Here  $\beta$  is the effective quadrupole polarizability of the target atom. The effective quadrupole polarizability comprises two terms: the adiabatic quadrupole interaction and the non-adiabatic dipole interaction, which in general are opposite in sign and of almost the same magnitude.

Substituting Equations (4) and (10) for two or three first partial waves (and Equation (12) for higher partial waves) into Equations (5)–(7) one gets relations which can be fitted to experimental data in order to determine the unknown parameters ( $b_l$  and  $R_l$ ) of the effective range expansion of  $B_l(k)$ .

## 2.2. Rigid Sphere Approach

In the rigid sphere model, the interaction potential between the charged particle and the neutral polarizable atom has the following form:

$$V(r) = \begin{cases} \infty, & r < r_0 \\ -\alpha e^2 / 2r^4, & r > r_0 \end{cases} \quad (16)$$

where  $r_0$  is the radius of rigid sphere.

Since the radial Schrödinger equation for the potential  $V(r)$  can be solved exactly using Mathieu functions, we showed in reference [27] that the expression for the scattering phase-shift of  $l^{\text{th}}$  partial wave takes a following form:

$$\tan \eta_l = \frac{\sin \delta_l - [C_l m_l^2 + \cot(\pi \nu_l)(m_l^2 - 1)] \cos \delta_l}{\cos \delta_l + [C_l m_l^2 + \cot(\pi \nu_l)(m_l^2 - 1)] \sin \delta_l}, \quad (17)$$

where  $m_l$ ,  $\nu_l$  and  $\delta_l$  are the same parameters as in Equation (4). Energy-dependent parameter  $C_l(k)$  can be determined from the continuity conditions imposed on the Mathieu functions at  $r = r_0$  (see [27] for more details). The only adjustable parameter is  $r_0$ , the radius of the rigid sphere.

For a potential in Equation (16) the  $s$ -wave scattering length can be described analytically as a function of dipole polarizability ( $\alpha$ ) and the radius of the hard-sphere ( $r_0$ ) as [29]:

$$A_0 = \sqrt{\alpha} \cot \left( \frac{\sqrt{\alpha}}{r_0} \right). \quad (18)$$

Integral elastic ( $\sigma_{IE}$ ), momentum transfer ( $\sigma_{MT}$ ), and differential elastic ( $d\sigma/d\omega$ ) cross-sections can be calculated using Equations (5)–(7).

## 3. Results

### 3.1. MERT

One can use nonlinear least-square regression procedures to fit MERT to chosen cross-section datasets and determine unknown parameters in the effective range approximation given by Equation (10). However, due to the multiparameter nature of the model, it seems to be more appropriate to use a Bayesian statistical inference for parameter estimation [30]. In contrast to the classical fitting, the Bayesian inference does not provide single point estimation in parameter space but rather the probability density functions (PDFs) of model parameters whose final form is shaped by (experimental or theoretical) observational data. Once posterior PDFs for each parameter are known, it is useful to provide a point estimation representing “best-fit” values together with an estimate of its errors. It can be done using either the mode or the mean value of PDF with the variance of distribution representing its uncertainty [30]. Generally, the larger the standard deviation of the parameter, the less sensitive model is to the changes of this parameter. Alternatively, one can give a credible region representing the predictive probability limit of the model due to parameters uncertainties (see [30] or [31] for a definition of this quantity).

Bayesian parameter estimation requires the computation of multi-dimensional integrals; a good solution for this computational problem consists of implementing Markov Chain Monte Carlo (MCMC) methods [30]. MCMC algorithms using prior PDF and likelihood functions generate a sequence of model parameters from a Markov Chain whose final stationary distribution is a desired posterior distribution. Here we adapt the MCMC Matlab toolbox by M. Laine [32] containing the Delayed Rejection and Adaptive Metropolis (DRAM) sampling algorithm with multivariate Gaussian proposal distributions introduced by Haario and co-workers [33]. We assume a Gaussian likelihood and (uninformative) prior PDF functions.

We choose available experimental total cross-sections (TCS) and momentum transfer cross-sections (MTCS) below the ionization threshold as the observational data. TCS are

measured usually in the most accurate (and absolute) way using electron beam techniques (where electron collisions with single atoms are studied), while MTCS are derived indirectly from the measurements of swarm transport parameters (where a cloud of electrons drifting in an external electric field through dense atomic gas is investigated). Below the ionization energy, TCS correspond to integral elastic cross-sections described by Equation (5), while MTCS are given by Equation (6). To check the predictive capabilities of the present model, the mean values of MERT parameters are used to calculate differential cross-sections (DCS, Equation (7)) and compare with experiments. DCS are more sensitive than TCS and MTCS to the correct values of the scattering phase-shift, so the comparison with the experimental DCS is a good test for the correctness of the model.

### 3.1.1. Helium

In Figure 1a,b we show an example of Markov Chains ( $10^6$  steps) for MERT parameters and corresponding posterior PDFs obtained by fitting the model to experimental TCS for electron–helium scattering by Buckman and Lohmann [34]. It was verified that below the ionization threshold (24 eV) only two first partials waves ( $l = 0$  and  $l = 1$ ) are distorted by the short-range interaction. Consequently, only four MERT coefficients ( $b_0, R_0, b_1,$  and  $R_1$ ) were used as the fitting parameters. The solid line in Figure 1c shows the MERT model using mean values of determined PDFs, while the darkened gray area represents a 99% prediction interval.

Similar MCMC fits were done to other data including TCS by Szmytkowski et al. [35] and Shigemura et al. [36], as well as MTCS data available in the LXCat database: <https://nl.lxcat.net/home/> (accessed on 1 August 2021). The latter data source includes calculations from S.F. Biagi’s FORTRAN code Magboltz 8.97 [37], the IST Lisbon dataset, [38], and the Morgan dataset [39]. The mean values and standard deviations of MERT parameters are given in Table 1. In all studied cases, both PDFs for  $b_0$  and  $R_0$  parameters are characterized by relatively narrow standard deviations, however only  $b_0$  mean values are comparable with each other. Although mean  $R_0$  differs between fits, its values are relatively small, not far from zero. It suggests that the short-range interaction is rather weakly dependent on incident electron energy below the ionization threshold and the scattering is strongly governed by the scattering length alone ( $A_0$ ). Large standard deviations for  $b_1$  and  $R_1$  demonstrate that model is weakly sensitive to both parameters. It reflects a small contribution of  $p$ -wave to the scattering process in almost the entire considered energy range. Although the  $p$ -wave phase shift increases slowly with electron energy, its contribution to cross-sections reaches of only about 20% at 20 eV i.e., the maximum energy considered. Consequently, it is difficult to determine  $b_1$  and  $R_1$  more precisely.

**Table 1.** Mean values and standard deviations of MERT parameters (appearing in the effective range approximation, Equation (10)) for  $e^- + \text{He}$  elastic scattering. The results were calculated using the dipole polarizability  $\alpha = 1.407 a_0^3$  [40] and the effective quadrupole polarizability  $\beta = 0.0 a_0^5$ .

Data	$A_0(a_0)$		$R_0(a_0)$		$b_1$		$R_1(a_0)$	
	Mean	Std	Mean	Std	Mean	Std	Mean	Std
TCS ( $1 \times 10^{-1}$ –20 eV) [34]	1.177	0.002	−0.058	0.015	−139	520	6	501
TCS ( $5 \times 10^{-1}$ –20 eV) [35]	1.174	0.003	0.085	0.017	−86	519	−95	511
TCS ( $6 \times 10^{-3}$ –20 eV) [36]	1.189	0.002	0.006	0.020	−90	528	−98	511
MTCS ( $1 \times 10^{-4}$ –20 eV) [37]	1.180	0.003	0.132	0.034	−42	488	−91	475
MTCS ( $2 \times 10^{-1}$ –20 eV) [38]	1.183	0.005	0.088	0.037	17	26	−10	34
MTCS ( $1 \times 10^{-2}$ –20 eV) [39]	1.186	0.002	0.146	0.020	34	359	−87	440

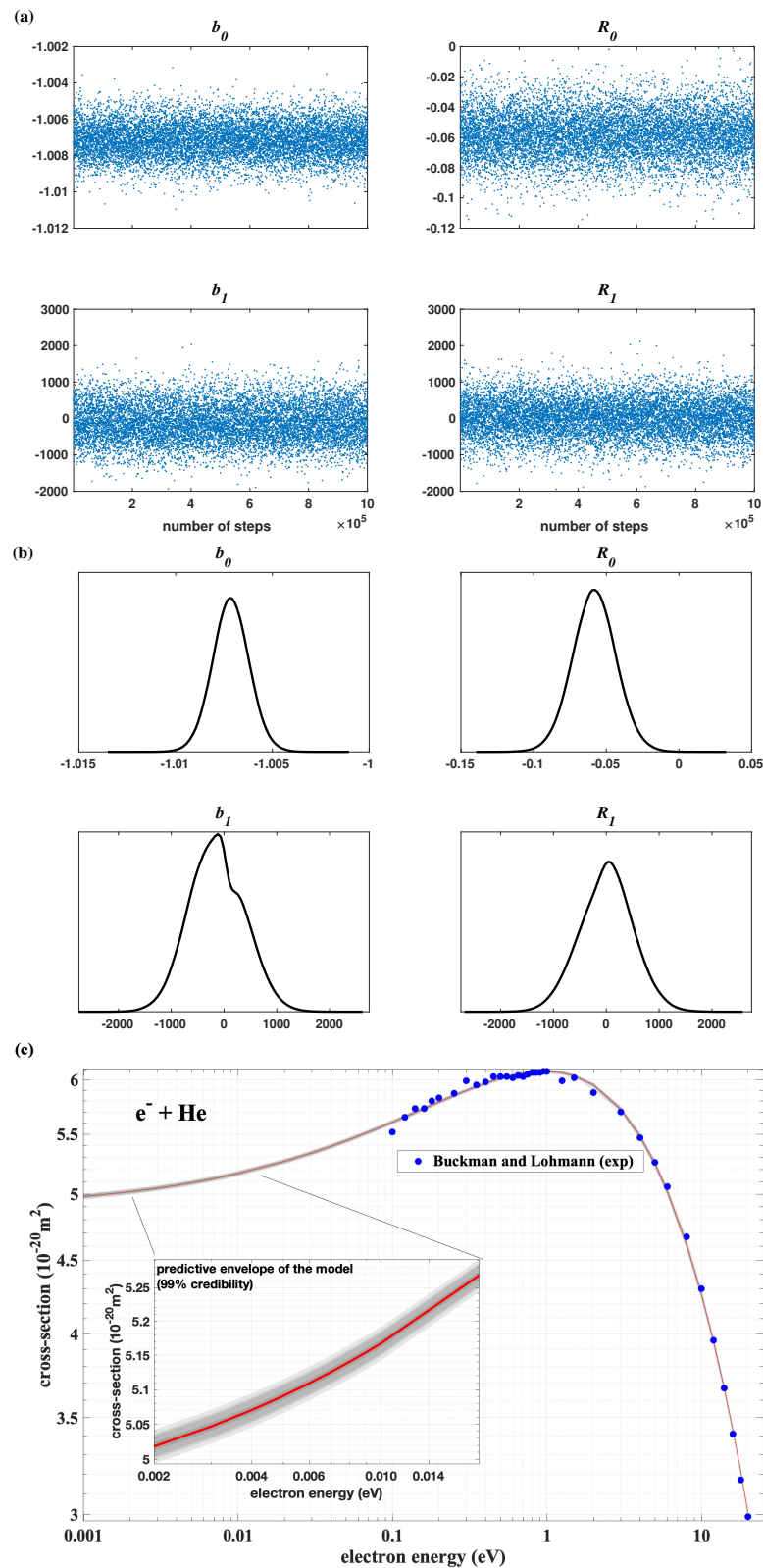


**Figure 1.** MCMC–MERT fit to experimental total cross–sections for electron–helium scattering by Buckman and Lohmann [34]: (a) Markov Chains for MERT parameters ( $b_0, R_0, b_1, R_1$ ) determined during the fitting procedure. (b) Posterior probability density functions (PDFs) for MERT parameters estimated from Markov Chains. (c) MERT calculations using mean values of PDFs (solid line) and a 99% credible region (darkened gray area).

Interestingly,  $b_0$  is very close to  $-1$  in all fits (see Markov chains and PDFs in Figure 1a,b), it implies that the  $s$ -wave scattering length for He is numerically equal (within the error of the analysis) to the square root of dipole polarizability in atomic units:  $A_0 \approx \sqrt{\alpha e^2 \mu / \hbar^2}$ . Note however that this also corresponds to the position of the maximum value of the  $p$ -wave centrifugal barrier, see Figure 2. In other words, the position of the maximum of the repulsive long-range potential for  $p$ -wave determines effective spatial boundaries of the target seen by low-energy electrons when colliding with the He atom.

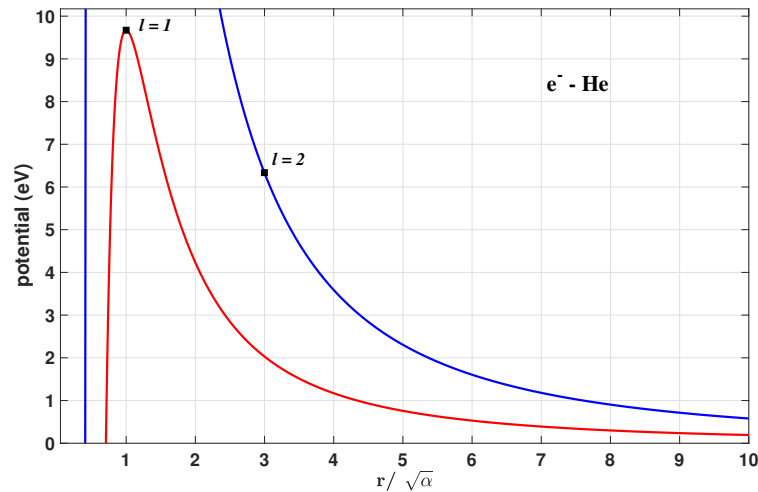


**Figure 2.** The positive (repulsive) part of the long-range electron–helium effective potentials for the  $p$  and  $d$  partial waves. The distance between interacting elements is scaled by the square root of dipole polarizability (in atomic units).

The MERT results are compared with experimental DCS in Figure 3. It is clear that the agreement is good. It proves that  $e^-$ –He elastic scattering below the ionization threshold is governed mainly by the  $s$ -wave scattering length. The latter quantity is equal approximately to the square root of dipole polarizability of the He atom (in atomic units).

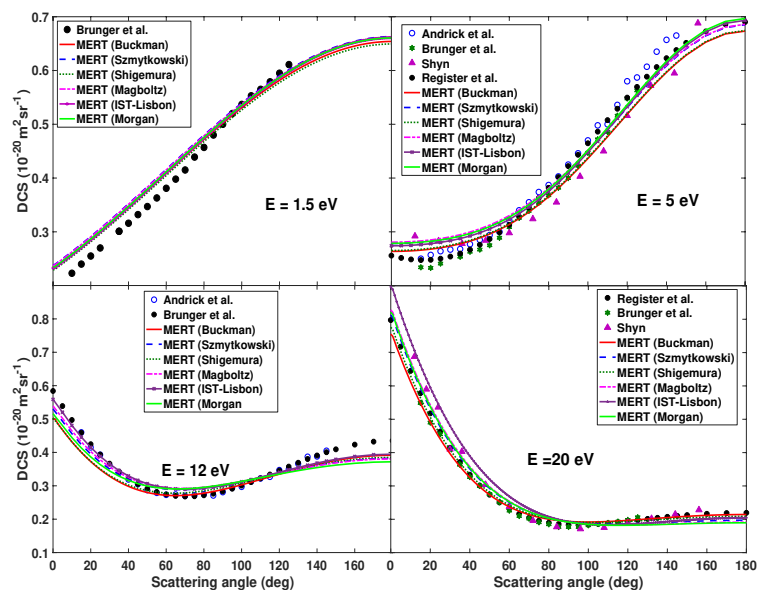


**Figure 3.** Angular dependencies of MERT–derived differential cross–sections at 1.5, 5, 12, and 20 eV for  $e^-$ –He scattering. The present results are compared with experimental data of Brunger et al. [41], Andrick et al. [42], Register et al. [43], and Shyn [44].

### 3.1.2. Neon

Similar MCMC–MERT analysis as for He has been done for other noble gases. For neon (Ne), TCS have been measured by many research groups below the threshold (16 eV) for the first Feshbach resonance (see references in [1,35]). Generally, good quality MERT fits can be achieved for many data. However, we found that only TCS by Szmytkowski et al. [35] and Shigemura et al. [36] covers enough wide energy range with sufficient resolution to determine MERT parameters confidently for both  $s$  and  $p$  partial waves. Both partial waves provide major contributions to the scattering cross-sections in the considered energy range. In the present analysis we take into account also swarm-derived MTCS from the LXCat database. This includes data by Puech [45], Morgan [39], Siglo [46], Robertson [47], and Magboltz 8.9 [37]. The results of MCMC–MERT fits are given in Table 2. For comparison, we also present the results of simultaneous MERT fit (using nonlinear least-squares regression) to the large collection of TCS datasets reported in [24].

This time, unlike for He, fitting the model to different datasets provide similar spreads of  $A_0$  and  $b_1$  mean values. Moreover, the  $R_0$  parameter is positive in all cases, and it is much larger than for helium. On the other hand, the  $R_1$  coefficient is small (it varies close to zero for different datasets). Hence the contribution of short-range interaction to the  $p$ -wave scattering is rather weakly dependent on the incident electron energy. Large standard deviations for  $b_2$  and  $R_2$  demonstrate that the model is weakly sensitive to both parameters since the contribution of  $d$ -wave to the scattering process is relatively small in almost the entire considered energy range (though not negligible at the upper part of the energy range).

In Figure 4 we compare MERT DCS with experimental data. In general, the agreement is good except for calculations using MERT parameters obtained from MTCS of Puech [45]. The discrepancy increases with the energy. This suggests that the interplay between the MERT parameter for  $p$  and  $d$  partial waves in this particular case is not correct.

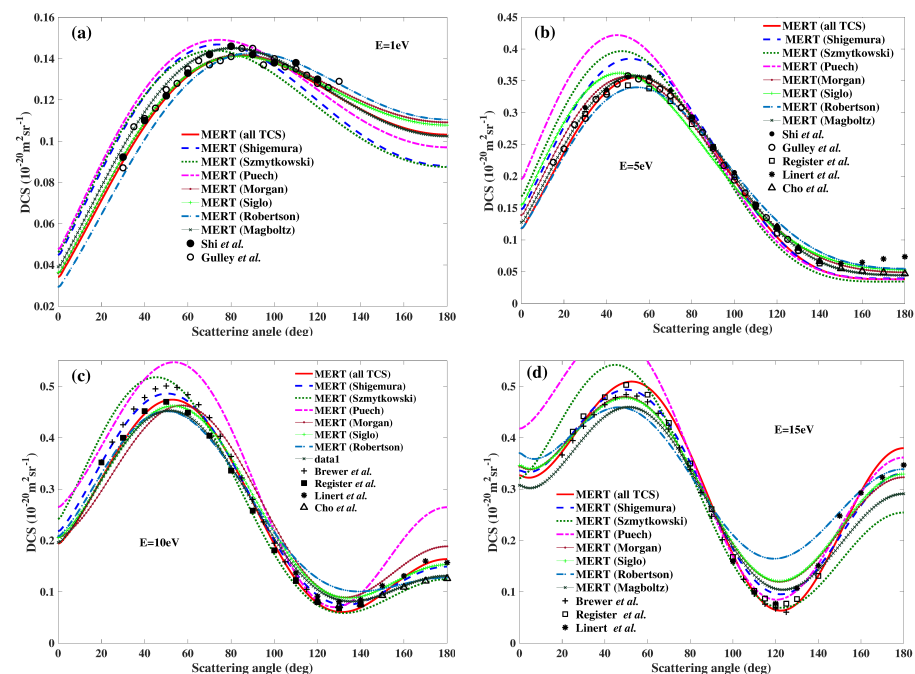


**Figure 4.** Angular dependencies of MERT–derived differential cross–sections at (a) 1, (b) 5, (c) 10, and (d) 15 eV for  $e^-$ –Ne scattering. The present results are compared with experimental data of Shi and Burrow [48], Linert et al. [49], Cho et al. [50], Register and Trajmar [43], Gulley et al. [51], and Szmytkowski et al. [35].

**Table 2.** Mean values and standard deviations of MERT parameters (appearing in the effective range approximation, Equation (10)) for  $e^- + \text{Ne}$  elastic scattering. The results were calculated using the dipole polarizability  $\alpha = 2.571 a_0^3$  [40] and the effective quadrupole polarizability  $\beta = 0.0 a_0^5$  [20].

Data	$A_0(a_0)$		$R_0(a_0)$		$b_1$		$R_1(a_0)$		$b_2$		$R_2(a_0)$	
	Mean	Std	Mean	Std	Mean	Std	Mean	Std	Mean	Std	Mean	Std
TCS ( $7 \times 10^{-3}$ –16 eV) [36]	0.228	0.004	3.710	1.970	−0.192	0.014	−0.080	0.054	−1	50	1	50
TCS ( $5 \times 10^{-1}$ –16 eV) [35]	0.225	0.007	1.955	4.18	−0.192	0.013	−0.042	0.030	0.228	501	6	501
all TCS ( $7 \times 10^{-3}$ –16 eV) [24]	0.227	-	3.697	-	−0.231	-	−0.028	-	0.001	-	0.361	-
MTCS ( $1 \times 10^{-4}$ –16 eV) [45]	0.241	0.002	3.652	0.180	−0.201	0.004	0.001	0.016	−0.472	40	1	50
MTCS ( $1 \times 10^{-2}$ –16 eV) [39]	0.228	0.003	4.674	0.162	−0.225	0.007	−0.063	0.023	−0.455	48	1	49
MTCS ( $3 \times 10^{-2}$ –20 eV) [46]	0.226	0.002	4.779	0.160	−0.223	0.005	−0.067	0.022	−0.235	46	0.722	48
MTCS ( $3 \times 10^{-2}$ –7 eV) [47]	0.222	0.001	5.93	0.220	−0.239	0.004	0.074	0.026	−0.101	47	2	50
MTCS ( $1 \times 10^{-4}$ –16 eV) [37]	0.224	0.001	3.596	0.366	−0.212	0.005	−0.090	0.014	0.008	0.055	0.436	0.25

### 3.1.3. Argon

In the case of argon (Ar), we found that the trustworthy MERT parameters can be obtained from the fits to TCS by Buckman and Lohmann [34], Ferch et al. [15], and Kurokawa et al. [52]. All of these datasets cover almost a full region of Ramsauer–Townsend minimum. In addition we verified that the following swarm-derived MTCS (from the LXCat database) can be analyzed confidently with MERT: Puech [45], Morgan [39], IST-Lisbon [38], Hayashi [53], and Magboltz 8.9 [37]. The results of MCMC–MERT fits are given in Table 3. Similar to Ne, both  $A_0$  and  $b_1$  are comparable for different datasets. However, the mean values of other MERT parameters ( $R_0$ ,  $R_1$ ,  $R_2$ , and  $b_2$ ) are characterized by some spread, which prevents the determination of a confidence interval for these parameters. Nevertheless, most of the MERT parameters provide DCS that are in excellent agreement with experimental data, as shown in Figure 5. The exception is the fit to Puech dataset [45], where too much uncertainty for the  $d$  wave parameters is obtained and, consequently, the compliance with the measurements is lower.

**Table 3.** Mean values and standard deviations of MERT parameters (appearing in the effective range approximation, Equation (10)) for  $e^- + \text{Ar}$  elastic scattering. The results were calculated using the dipole polarizability  $\alpha = 11.23 a_0^3$  [40] and the effective quadrupole polarizability  $\beta = 0.0 a_0^5$  [20].

Data	$A_0(a_0)$		$R_0(a_0)$		$b_1$		$R_1(a_0)$		$b_2(a_0)$		$R_2(a_0)$	
	Mean	Std	Mean	Std	Mean	Std	Mean	Std	Mean	Std	Mean	Std
TCS ( $1.2 \times 10^{-1}$ –10 eV) [34]	−1.500	0.010	−0.427	0.153	−0.448	0.011	0.072	0.037	0.206	0.001	0.315	0.014
TCS ( $8 \times 10^{-2}$ –10 eV) [15]	−1.490	0.010	−0.142	0.010	−0.496	0.010	0.188	0.025	1.075	0.238	−0.272	0.175
all TCS ( $7 \times 10^{-3}$ –10 eV) [52]	−1.400	0.010	−0.661	0.150	−0.463	0.016	0.130	0.046	0.339	0.092	0.213	0.065
MTCS ( $1 \times 10^{-3}$ –10 eV) [37]	−1.460	0.010	0.101	0.167	−0.437	0.005	−0.198	0.054	0.069	0.022	0.425	0.012
MTCS ( $1 \times 10^{-2}$ –10 eV) [53]	−1.490	0.010	0.845	0.472	−0.456	0.009	−0.017	0.163	0.206	0.136	0.317	0.104
MTCS ( $1 \times 10^{-3}$ –10 eV) [38]	−1.560	0.010	1.557	0.198	−0.471	0.036	0.074	0.143	1.043	0.484	−0.305	0.394
MTCS ( $3 \times 10^{-3}$ –10 eV) [39]	−1.490	0.010	1.189	0.044	−0.451	0.007	0.077	0.028	0.699	0.065	−0.063	0.054
MTCS ( $1 \times 10^{-4}$ –10 eV) [45]	−1.570	0.020	1.742	0.396	−0.510	0.058	0.322	0.164	7.55	19.56	−5.53	15.92

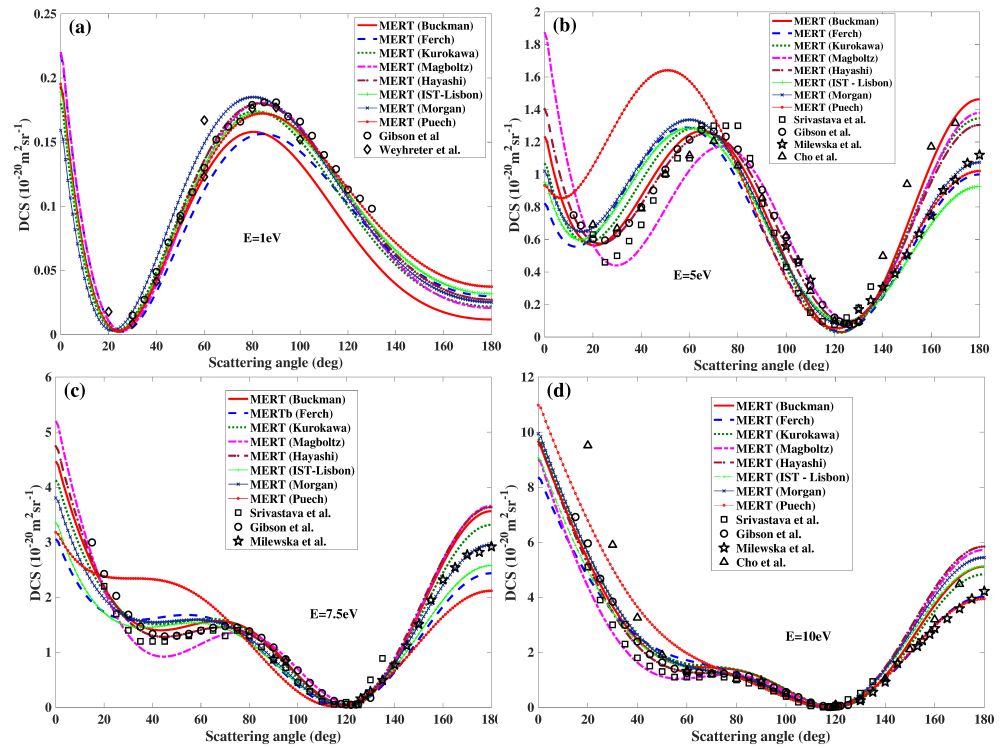


**Figure 5.** Angular dependencies of MERT–derived differential cross–sections at (a) 1, (b) 5, (c) 7.5, and (d) 10 eV for  $e^-$ –Ar scattering. The present results are compared with experimental data of Gibson et al. [54], Weyhreter et al. [55], Cho and Park [56], Srivastava et al. [57], and Milewska et al. [58].

### 3.1.4. Krypton

We analyzed a huge amount of available experimental TCS [35,52,59–61] and MTCS [37,39,46,62–67] for krypton (Kr) at low energies. We found that the fits to only three datasets (Buckman [59], Jost [61] and Hunter [64]) provide trustworthy MERT parameters that allow reconstructing experimental DCS below 10 eV. The results of fits are given in Table 4. For comparison, we also show the results of MERT fit (see [23]) to DCS measured with the magnetic-field angle analyzer, as reported by Zatsarinny et al. [68]. This experimental technique allows DCS measurements in full angular range (from 0° to 180°). Moreover, the data of Zatsarinny et al. [68] were obtained in a vast energy range with incredibly high resolution (15 meV). Consequently, as we showed in [23], the MERT parameters can be extracted quite accurately.

Similar to Ne and Ar, both  $A_0$  and  $b_1$  are comparable for all four datasets. Other MERT parameters are determined with much lower accuracy but still provide relatively good agreement with experimental DCS (see Figure 6).

**Table 4.** Mean values and standard deviations of MERT parameters (appearing in the effective range approximation, Equation (10)) for  $e^-$ +Kr elastic scattering. The results were calculated using the dipole polarizability  $\alpha = 16.86 a_0^3$  [40] and the effective quadrupole polarizability  $\beta = 8.0 a_0^5$  [20].

Data	$A_0(a_0)$		$R_0(a_0)$		$b_1$		$R_1(a_0)$		$b_2(a_0)$		$R_2(a_0)$	
	Mean	Std	Mean	Std	Mean	Std	Mean	Std	Mean	Std	Mean	Std
TCS (0.175–10 eV) [59]	−3.280	0.010	−0.509	0.068	−0.552	0.010	0.054	0.026	0.267	0.011	0.466	0.118
TCS (0.3–10 eV) [61]	−3.380	0.030	0.929	0.077	−0.664	0.012	0.121	0.027	0.249	0.019	0.503	0.026
DCS (<10 eV) [23]	−3.480	-	0.533	-	−0.599	-	0.125	-	0.039	-	0.720	-
MTCS (0.1–8 eV) [64]	−3.380	0.020	0.340	0.128	−0.527	0.030	−0.389	0.111	0.099	0.041	0.608	0.022

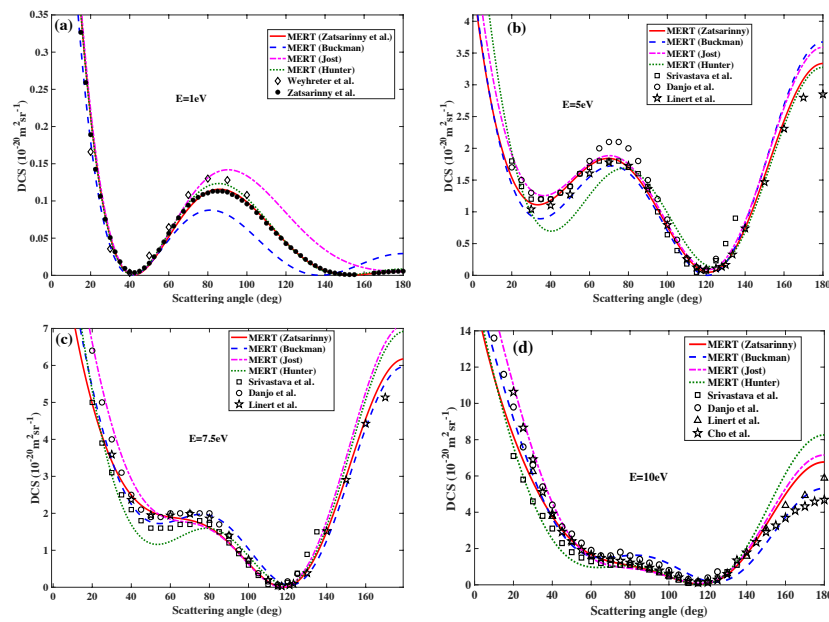


**Figure 6.** Angular dependencies of MERT–derived differential cross–sections at (a) 1, (b) 5, (c) 7.5, and (d) 10 eV for  $e^-$ –Kr scattering. The present results are compared with experimental data of Srivastava et al. [57], Danjo [69], Linert et al. [70], Cho et al. [71], Weyhreter et al. [55], and Zatsarinny et al. [68].

### 3.1.5. Xenon

The MCMC–MERT analysis of experimental TCS data for Xenon (Xe) has already been reported in [25]. In Table 5 we give only those MERT parameters that allow reconstructing experimental DCS below 10 eV. The most recent experimental TCS of Kurokawa et al. [52], and older measurements by Alle et al. [72] and Guskov et al. [73] are not included in the present analysis because the fits to these cross-sections do not provide correct DCS. Additionally, in the present work, we analyzed different MTCS [37,45,62,64,66,74], however only the fit to data by Hayashi [75] is consistent with DCS. For comparison, we also present in Table 5 the results of simultaneous robust MERT fit to all available TCS (using MATLAB routine for nonlinear least-square regression of multiple data sets) done in reference [25].

Since the  $d$ -wave plays an important role in  $e^- + \text{Xe}$  elastic scattering below 10 eV, it is much easier to determine MERT coefficients associated with this partial wave than for other noble gases. Consequently, this time all three parameters  $A_0$ ,  $b_1$ , and  $b_2$  are comparable between different sets given in Table 5. Moreover, even  $R_2$  values are also of the same order. However, the spreads of  $R_0$  and  $R_1$  are too large to estimate the confidence intervals for both of them. Nevertheless, such uncertainties in both parameters do not have an important influence on DCS calculations, which are in good agreement with experiments (see Figure 7).

**Table 5.** Mean values and standard deviations of MERT parameters (appearing in the effective range approximation, Equation (10)) for  $e^- + \text{Xe}$  elastic scattering. The results were calculated using the dipole polarizability  $\alpha = 27.04 a_0^3$  [40] and the effective quadrupole polarizability  $\beta = 16.8 a_0^5$  [17].

Data	$A_0(a_0)$		$R_0(a_0)$		$b_1$		$R_1(a_0)$		$b_2(a_0)$		$R_2(a_0)$	
	Mean	Std	Mean	Std	Mean	Std	Mean	Std	Mean	Std	Mean	Std
TCS (0.125–10 eV) [60]	−6.510	0.050	−0.136	0.163	−0.690	0.048	0.023	0.040	0.220	0.035	0.593	0.040
TCS (0.2–10 eV) [61]	−6.870	0.011	−0.484	0.376	−0.670	0.082	0.232	0.057	0.170	0.083	0.663	0.071
TCS (0.5–10 eV) [35]	−6.750	0.500	0.462	0.526	−0.630	0.127	0.023	0.074	0.290	0.100	0.644	0.095
all TCS (0.5–10 eV) [25]	−6.490	-	0.097	-	−0.680	-	−0.019	-	0.200	-	0.668	-
MTCS (0.001–10 eV) [53]	−6.210	0.010	−0.043	0.181	−0.775	0.097	0.163	0.051	0.184	0.135	0.810	0.113

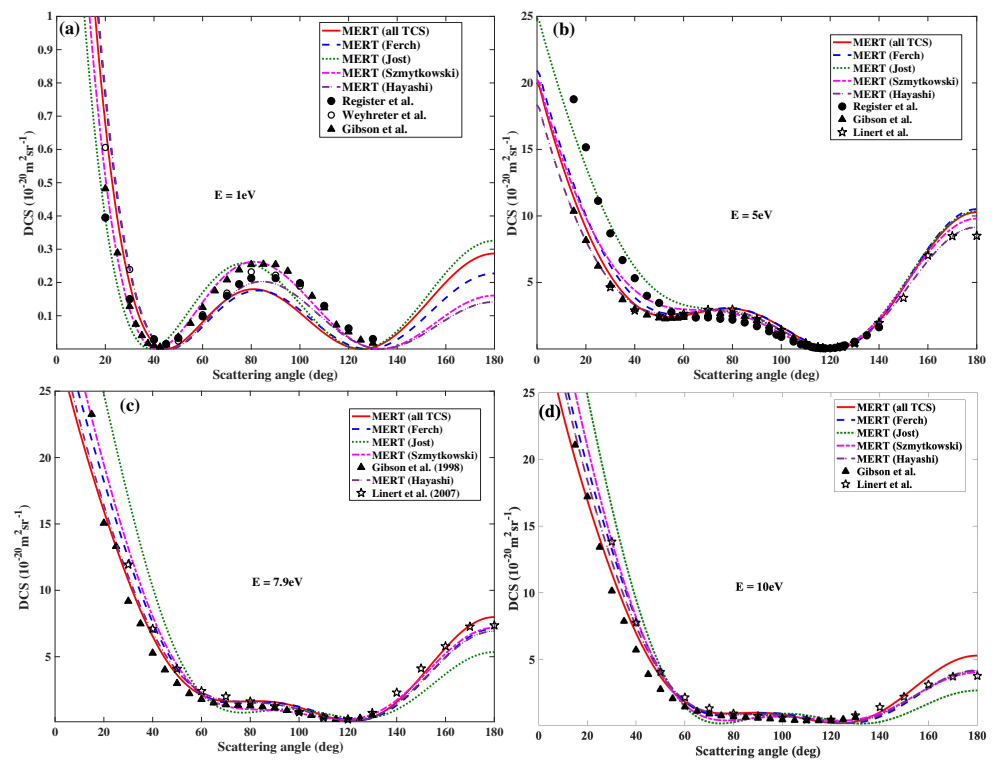


**Figure 7.** Angular dependencies of MERT–derived differential cross–sections at (a) 1, (b) 5, (c) 7.9, and (d) 10 eV for  $e^-$ –Xe scattering. The present results are compared with experimental data of Register et al. [76], Gibson et al. [77], Linert et al. [78], and Weyhreter et al. [55].

### 3.1.6. MERT Parameters

In Figure 8a, we show MERT-derived scattering length versus the dipole polarizability. We use values averaged over coefficients determined in MCMC–MERT analysis of different datasets (Tables 1–5). The standard deviations of the mean values are used to indicate the uncertainties in the determination of coefficients. For Ar, Kr, and Xe, the attractive polarization potential overcomes the repulsive exchange interaction due to relatively large dipole polarizabilities. Consequently, the scattering length is negative, and it changes linearly with polarizability (as shown by the dashed line). On the other hand, for He and Ne, the repulsive interaction with electrons is slightly dominant, making the scattering length positive, and a small deviation from the linear dependency  $A_0(\alpha)$  is observed.

In Figure 8b, we plot the zero-energy contribution ( $b_1$ ) of the short-range potential to the  $p$ -wave scattering phase-shift versus dipole polarizability. A clear regular tendency is observed,  $b_1$  becomes more negative with increasing polarizability. We do not give a  $b_1$  for helium due to the high uncertainties in MCMC–MERT analysis (see Table 1). However, the observed tendency suggests that this parameter is small (close to zero) for He.

Unfortunately, we can not make a similar plot for the  $b_2$  parameter (i.e., the zero-energy contribution of short-range potential to the  $d$ -wave phase shift) due to too high uncertainty related to this coefficient. Nevertheless, a careful inspection of data from Tables 3–5 (Ar, Kr, and Xe) shows that, unlike  $b_1$ , the  $b_2$  parameter is always positive.

Similarly to the  $b_2$  parameter, the “effective ranges” ( $R_0$ ,  $R_1$ , and  $R_2$ ) can not be estimated accurately and they vary depending on the dataset used for analysis. Clearly, the effective-range corrections are relatively small in the low-energy regime in comparison to the leading contributions due to the  $s$ -wave scattering length, the  $p$ -wave, and the  $d$ -wave zero-energy contributions. Consequently, the effective-range parameters are strongly affected by measurement uncertainties in the experimental data in the low-energy domain. Extending the energy range to higher energies in MERT analysis does not work since the effective-range approximation (Equation (10)) becomes less accurate with increasing electron energy. Nevertheless, the present results show that the effective-range corrections

may be comparable with leading contributions in the case of *s*-wave for Ne and *d*-wave for Xe, where the corresponding  $R_l$  values, obtained from different fits, are of the same order of magnitude.

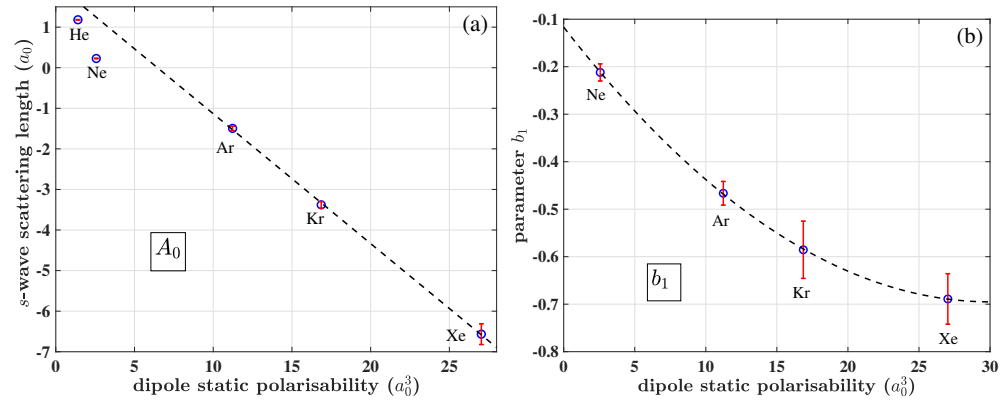


**Figure 8.** (a) MERT-derived *s*-wave scattering lengths and (b) parameter  $b_1$  for rare gases plotted versus static dipole polarizability. The presented results are the mean values of MCMC–MERT analysis of different experimental cross-section datasets. The standard deviations of mean values are given to demonstrate the uncertainties in the determination of coefficients. The dashed lines are sketched as the guide to eyes to show general tendencies in  $A_0(\alpha)$  and  $b_1(\alpha)$  dependencies.

### 3.2. Rigid Sphere Model

The rigid sphere model requires the proper choice of the hard-core radius  $r_0$ . We found [27] that for positron scattering on noble gases, the  $r_0$  corresponds to the positions of the principal maxima in the radial distributions of outermost atomic orbitals. It reflects the fact that the positron does not penetrate far inside the atom due to the strong repulsive static potential (that can be modeled as the hard core). The first attempt to apply a similar model for electron scattering was done by Reisfeld and Asaf [79] who proposed to use the atomic radii calculated from the van der Waals equations of state as the hard-core radii. They aimed to describe the scattering length for electron interaction with noble gases as a function of atomic dipole polarizability. However, such a choice of radii was criticized by R. Szmytkowski [80] who proved its incorrectness. If the rigid sphere model applies, we can benefit from Equation (18) relating  $r_0$  with the scattering length. In our calculations we use mean values of the scattering length ( $\langle A_0 \rangle$ ) determined in the present MERT analysis. Such a choice of  $r_0$  determination gives negative radii for Ar, Kr, and Xe. This is obviously an unphysical outcome, limiting our analysis only to He and Ne, where  $r_0$  is positive. Interestingly, a similar discrepancy between negative- and positive-scattering-length gases was noticed in multiple-scattering theories [81] describing electron interaction with dense gases. To solve this problem, Borghesani et al. [81–83] developed a hard-sphere-like model for electron multiple-scattering.

All parameters used in the present model are given in Table 6. The  $r_0$  for electrons is much higher than the corresponding values for positrons [27]. It may be due to the different nature of the repulsive potential for both particles: positrons are repelled by static interactions while electrons are repulsed by the exchange potential.

**Table 6.** Parameters used in the rigid sphere model: the dipole polarizability ( $\alpha$ ), the mean value of the scattering length determined in the present MERT analysis ( $\langle A_0 \rangle$ ), and the rigid sphere radius ( $r_0$ ) determined from Equation (18).

Atom	$\alpha (a_0^3)$	$\langle A_0 \rangle (a_0)$	$r_0 (a_0)$
He	1.407	1.181	1.50
Ne	2.671	0.228	1.14

In Figures 9 and 10 we show the scattering phase-shifts of  $s$ ,  $p$ , and  $d$ -waves as well as the integral elastic cross-sections calculated using the rigid sphere model. Present results are compared with other theoretical and experimental determinations. For both gases, the model provides the  $s$ -wave and  $d$ -wave phase shifts that are in excellent agreement with other works to as high energy as 1 eV (for neon even up to 6 eV for  $s$ -wave). For  $p$ -wave, the agreement is worse; nonetheless, since its contribution is small compared to  $s$ -wave at low energies, the model can reconstruct experimental total cross-sections almost up to 1 eV for both atoms. This result suggests that in the case of He and Ne, the repulsive exchange potential felt by an incoming slow electron is sufficiently strong to be modeled by the infinitive barrier, while the attractive part of the potential (static and polarization) can be described effectively by the long-range  $r^{-4}$  interaction.

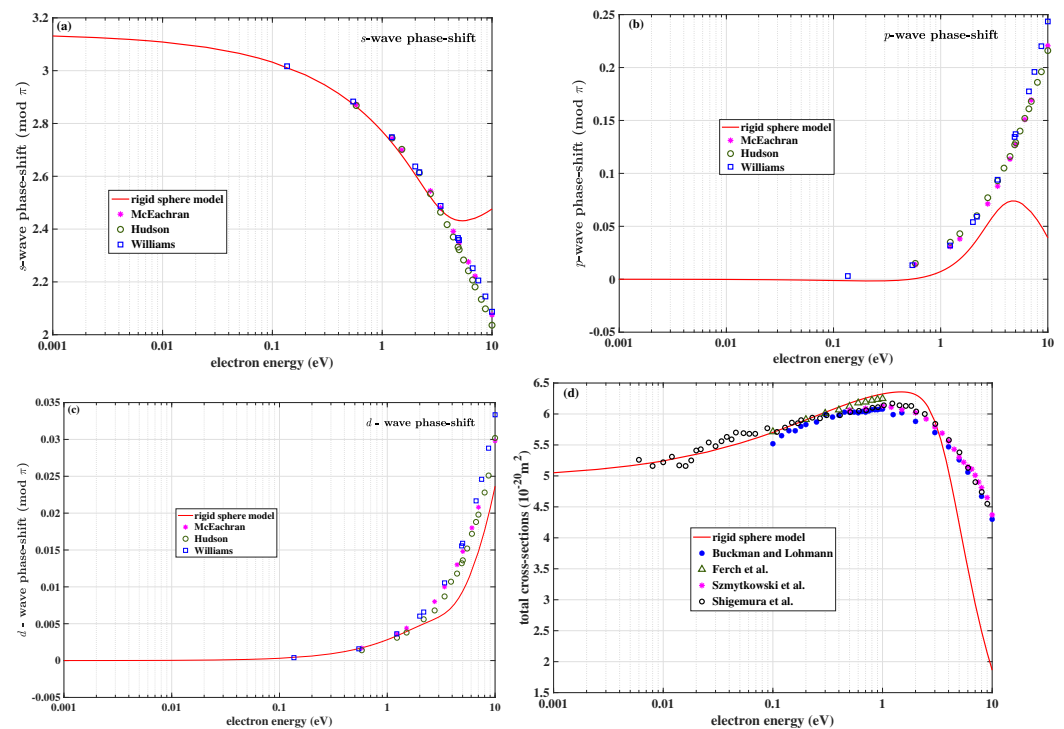


**Figure 9.** The rigid sphere model (solid lines) for low-energy  $e^-$ –He scattering: (a)  $s$ -wave phase-shift, (b)  $p$ -wave phase-shift, (c)  $d$ -wave phase-shift, and (d) integral elastic cross-sections. The model is compared with other works: phase-shifts by McEachran and Stauffer [84], Hudson et al. [85], and Williams [86]; total cross-sections by Buckman and Lohmann [34], Ferch et al. [87], Szmytkowski et al. [35], and Shigemura et al. [36].

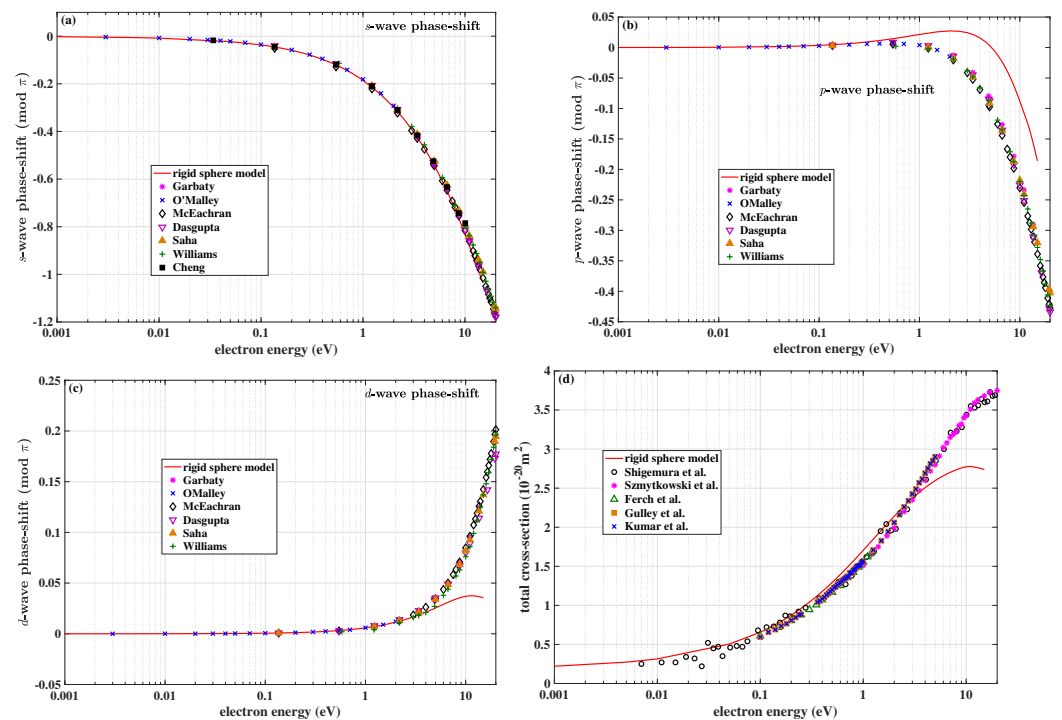


**Figure 10.** The rigid sphere model (solid lines) for low-energy  $e^-$ -Ne scattering: (a)  $s$ -wave phase-shift, (b)  $p$ -wave phase-shift, (c)  $d$ -wave phase-shift and (d) integral elastic cross-sections. The model is compared with other works: phase-shifts by Garbaty and LaBahn [88], O'Malley and Crompton [89], McEachran and Stauffer [90], Dasgupta and Bhatia [91], Saha [92], Williams [86], and Cheng et al. [18]; total cross-sections by Shigemura et al. [36], Szymtkowski et al. [35], Ferch et al. [93], Gulley et al. [51], and Kumar et al. [94].

#### 4. Summary

We performed an extensive MCMC-MERT analysis of cross-sections for electron scattering from noble gases in the present work. We analyzed many experimental datasets of integral cross-sections, including total and momentum transfer cross-sections (TCS and MTCS). We selected those experimental data that comply with the differential cross-sections (DCS) within the current model. This statistical analysis was done to determine the confidence ranges for the MERT parameters appearing in the effective-range expansion of the short-range potential. We found that both the  $s$ -wave scattering length and the  $p$ -wave leading contribution can be determined confidently from available data. We showed that both parameters change in a regular manner with the dipole polarizability of atomic targets. On the other hand, other MERT parameters, including the “effective ranges”, can not be determined with the same confidence. Nevertheless, some interesting tendencies can be spotted from the present study. In particular, the  $d$ -wave leading term seems to be positive for Ar, Kr, and Xe, where the  $d$ -wave contribution is not negligible below the threshold for the first inelastic process.

In the particular case of  $e^-$ -He scattering, we noticed that the  $s$ -wave scattering length is numerically equal to the square root of dipole polarizability of helium when expressed in atomic units. Interestingly, this also corresponds to the position of the maximum of the centrifugal potential barrier for the  $p$  partial wave. In other words, the repulsive part of  $p$ -wave interaction potential determines effective spatial boundaries of the helium atom “seen” by slow electrons. Similar correspondence is not observed for other noble gases.

We also verified the applicability of the rigid sphere model for low-energy electron interaction with noble gases. As could be expected, the hard-sphere model is roughly applicable for He and Ne only (which do not show the Ramsauer-Townsend minimum) since their integral cross-section changes slowly in the limit of zero energy (note also a similar approach for He by Borghesani in this issue [83]). The model can not be applied for

argon, krypton, and xenon, where the repulsive exchange interaction is not strong enough with respect to the attractive part of the interaction potential. Consequently, the repulsive part can not be modeled effectively by the infinitive wall.

Finally, we showed in this paper that MERT could describe cross-sections at low energies for such highly polarizable systems as Kr and Xe. The question remains if our model is also applicable for other atomic targets, for example, tungsten (W) and beryllium (Be). Knowledge of cross-sections of atoms (including metals) is decisive in modeling plasmas, particularly in thermonuclear reactors. In tokamak-like reactors, the temperature and plasma density in the case of carbon-lining of the walls are well predicted by the theoretical simulations. However, in the case of a W-lined reactor, the discrepancy between the measured and modeled densities is by a factor of three [95]. It is due to the lack of reliable cross-sections. The study of MERT applicability for other atoms is in progress.

**Funding:** This research received no external funding.

**Data Availability Statement:** Not applicable.

**Acknowledgments:** The author would like to thank Grzegorz Karwasz (Nicolaus Copernicus University in Torun, Poland) for helpful suggestions and discussions.

**Conflicts of Interest:** The author declares no conflict of interest. The funders had no role in the design of the study; in the collection, analyses, or interpretation of data; in the writing of the manuscript, or in the decision to publish the results.

## Abbreviations

The following abbreviations are used in this manuscript:

MCMC–MERT	Markov Chain Monte Carlo–Modified Effective Range Analysis
TCS	Total Cross–Sections
MTCS	Momentum Transfer Cross–Sections
DCS	Differential Cross–Sections
PDF	Probability Density Function
He	Helium
Ne	Neon
Ar	Argon
Kr	Krypton
Xe	Xenon

## References

1. Zecca, A.; Karwasz, G.P.; Brusa, R.S. One century of experiments on electron-atom and molecule scattering: A critical review of integral cross-sections. *Rev. Nuovo Cim.* **1996**, *19*, 3. [\[CrossRef\]](#)
2. Szmytkowski, C.; Mozejko, P. Recent total cross section measurements in electron scattering from molecules *Eur. Phys. J. D* **2020**, *74* 90.
3. Zatsarinny, O.; Bartschat, K. B-spline Breit–Pauli R-matrix calculations for electron collisions with neon atoms. *J. Phys. B* **2004**, *37*, 2173. [\[CrossRef\]](#)
4. Zatsarinny, O.; Bartschat, K. B-spline Breit–Pauli R-matrix calculations for electron collisions with argon atoms. *J. Phys. B* **2004**, *37*, 4693. [\[CrossRef\]](#)
5. Godyak, A.; Piejak, R.B. Abnormally low electron energy and heating-mode transition in a low-pressure argon rf discharge at 13.56 MHz. *Phys. Rev. Lett.* **1990**, *65*, 996. [\[CrossRef\]](#)
6. Song, M.-Y.; Yoon, J.-S.; Cho, H.; Itikawa, Y.; Karwasz, G.P.; Kokoouline, V.; Nakamura, Y.; Tennyson, J. Cross Sections for Electron Collisions with Methane. *J. Phys. Chem. Ref. Data* **2017**, *44*, 023101. [\[CrossRef\]](#)
7. Song, M.-Y.; Yoon, J.-S.; Cho, H.; Itikawa, Y.; Karwasz, G.P.; Kokoouline, V.; Nakamura, Y.; Tennyson, J. Cross Sections for Electron Collisions with Acetylene. *J. Phys. Chem. Ref. Data* **2017**, *46*, 013106. [\[CrossRef\]](#)
8. Bethe, H.A. Theory of the Effective Range in Nuclear Scattering. *Phys. Rev.* **1949**, *76*, 38. [\[CrossRef\]](#)
9. Blatt, J.M.; Jackson, J.D. On the interpretation of neutron-proton scattering data by the Schwinger Variational Method. *Phys. Rev.* **1949**, *26*, 18. [\[CrossRef\]](#)
10. O'Malley, T.F.; Spruch, L.; Rosenberg, L. Modification of EffectiveRange Theory in the Presence of a Long-Range ( $r^{-4}$ ) Potential. *J. Math. Phys.* **1961**, *2*, 491. [\[CrossRef\]](#)

11. Malley, T.F.O.; Spruch, L.; Rosenberg, L. Low-Energy Scattering of a Charged Particle by a Neutral Polarizable System. *Phys. Rev.* **1962**, *125*, 1300. [[CrossRef](#)]
12. O'Malley, T.F. Extrapolation of Electron—Rare Gas Atom Cross Sections to Zero Energy. *Phys. Rev.* **1963**, *130*, 1020. [[CrossRef](#)]
13. Mann, A.; Linder, F. Low-energy electron scattering from halomethanes. I. Elastic differential cross section for e-CF<sub>4</sub> scattering. *J. Phys. B At. Mol. Opt. Phys.* **1992**, *25*, 533. [[CrossRef](#)]
14. Lunt, S.L.; Randell, J.; Ziesel, J.-P.; Mrotzek, G.; Field, D. Very low energy electron scattering in some hydrocarbons and perfluorocarbons. *J. Phys. B At. Mol. Opt. Phys.* **1998**, *31*, 4225. [[CrossRef](#)]
15. Ferch, J.; Granitza, B.; Masche, C.; Raith, W. Electron-argon total cross section measurements at low energies by time-of-flight spectroscopy. *J. Phys. B* **1985**, *18*, 967. [[CrossRef](#)]
16. Karwasz, G.P.; Karbowski, A.; Idziaszek, Z.; Brusa, R.S. Total cross sections for positron scattering on benzene—Angular resolution corrections. *Nucl. Instrum. Methods Phys. Res. Sect. B* **2008**, *266*, 471. [[CrossRef](#)]
17. Kitajima, M.; Kurokawa, M.; Kishino, T.; Toyoshima, K.; Odagiri, T.; Kato, H.; Anzai, K.; Hoshino, M.; Tanaka, H.; Ito, K. Ultra-low-energy electron scattering cross section measurements of Ar, Kr and Xe employing the threshold photoelectron source. *Eur. Phys. J. D* **2012**, *66*, 130. [[CrossRef](#)]
18. Cheng, Y.; Tang, L.Y.; Mitroy, J.; Safronova, M.S. All-order relativistic many-body theory of low-energy electron-atom scattering. *Phys. Rev. A* **2014**, *89*, 012701. [[CrossRef](#)]
19. Green, D.; Ludlow, J.A.; Gribakin, G.A. Positron scattering and annihilation on noble-gas atoms. *Phys. Rev. A* **2014**, *90*, 032712. [[CrossRef](#)]
20. Buckman, S.J.; Mitroy, J. Analysis of low-energy electron scattering cross sections via effective-range theory. *J. Phys. B At. Mol. Phys.* **1989**, *22*, 1365. [[CrossRef](#)]
21. Idziaszek, Z.; Karwasz, G.P. Applicability of modified effective-range theory to positron-atom and positron-molecule scattering. *Phys. Rev. A* **2006**, *73*, 064701. [[CrossRef](#)]
22. Fedus, K.; Karwasz, G.P.; Idziaszek, Z. An analytic approach to modified effective range theory for electron and positron elastic scattering. *Phys. Rev. A* **2013**, *88*, 012704. [[CrossRef](#)]
23. Fedus, K. Modified effective range analysis of electron scattering from krypton. *Phys. Scr.* **2014**, *89*, 105401. [[CrossRef](#)]
24. Fedus, K. Electron Scattering from Neon Via Effective Range Theory. *Braz. J. Phys.* **2014**, *44*, 622. [[CrossRef](#)]
25. Fedus, K. Markov Chain Monte Carlo Effective Range Analysis of Low-Energy Electron Elastic Scattering from Xenon. *Braz. J. Phys.* **2016**, *46*, 1. [[CrossRef](#)]
26. Lun, D.R.; Amos, K.; Allen, L.J. Inversion of total and differential cross-section data for electron-methane scattering. *Phys. Rev. A* **1996**, *53*, 831. [[CrossRef](#)]
27. Fedus, K. A rigid sphere approach to positron elastic scattering by noble gases, molecular hydrogen, nitrogen and methane. *Eur. Phys. J. D* **2016**, *70*, 261. [[CrossRef](#)]
28. Ali, M.K.; Fraser, P.A. The contribution of long-range forces to low-energy phaseshifts. *J. Phys. B At. Mol. Phys.* **1977**, *10*, 3091. [[CrossRef](#)]
29. Szymkowski, R. Analytical calculations of scattering lengths in atomic physics. *J. Phys. A: Math. Gen.* **1995**, *28*, 7333. [[CrossRef](#)]
30. Gregory, P. *Bayesian Logical Data Analysis for the Physical Sciences*; Cambridge University Press: New York, NY, USA, 2005.
31. Fedus, K.; Franz, J.; Karwasz, G.P. Positron scattering on molecular hydrogen: Analysis of experimental and theoretical uncertainties. *Phys. Rev. A* **2015**, *91*, 062701. [[CrossRef](#)]
32. Laine, M. MCMC toolbox for Matlab, available online: <https://mjlaine.github.io/mcmcstat/> (accessed on 15 June 2021).
33. Haario, H.; Laine, M.; Mira, A.; Saksman, E. DRAM: Efficient adaptive MCMC. *Stat. Comput.* **2006**, *16*, 339. [[CrossRef](#)]
34. Buckman, S.J.; Lohmann, B. Low-energy total cross section measurements for electron scattering from helium and argon. *J. Phys. B At. Mol. Phys.* **1986**, *19*, 2547. [[CrossRef](#)]
35. Szymkowski, C.; Maciag, K.; Karwasz, G. Absolute electron-scattering total cross section measurements for noble gas atoms and diatomic molecules. *Phys. Scripta* **1996**, *54*, 271. [[CrossRef](#)]
36. Shigemura, K.; Kitajima, M.; Kurokawa, M.; Toyoshima, K.; Odagiri, T.; Suga, A.; Kato, H.; Hoshino, M.; Tanaka, H.; Ito, K. Total cross sections for electron scattering from He and Ne at very low energies. *Phys. Rev. A* **2014**, *89*, 022709. [[CrossRef](#)]
37. Fortran Program, MAGBOLTZ 8.9, S.F. Biagi, Sept 2011 (from LXcat database). Available online: <https://nl.lxcat.net/home/> (accessed on 1 August 2021).
38. Alves, L.L. The IST-Lisbon database on LXCat. *J. Phys. Conf. Ser.* **2014**, *565*, 1. [[CrossRef](#)]
39. Cross-Sections Assembled over the Course of 30 Years by WL Morgan—Suitable for Use with 2-Term Boltzmann Solvers. Available online: [www.lxcat.net/Morgan](http://www.lxcat.net/Morgan) (accessed on 1 August 2021).
40. Olney, T.N.; Cann, N.M.; Cooper, G.; Brion, C.E. Absolute scale determination for photoabsorption spectra and the calculation of molecular properties using dipole sum-rules. *Chem. Phys.* **1997**, *223*, 59. [[CrossRef](#)]
41. Brunger, M.J.; Buckman, S.J.; Allen, L.J.; McCarthy, I.E.; Ratnavelu, K. Elastic electron scattering from helium: Absolute experimental cross sections, theory and derived interaction potentials. *J. Phys. B* **1992**, *25*, 1823. [[CrossRef](#)]
42. Andrick, D.; Bitsch, A. Experimental investigation and phase shift analysis of low-energy electron-helium scattering. *J. Phys. B* **1975**, *8*, 393. [[CrossRef](#)]
43. Register, D.F.; Trajmar, S.; Srivastava, S.K. Absolute elastic differential electron scattering cross sections for He: A proposed calibration standard from 5 to 200 eV. *Phys. Rev. A* **1980**, *21*, 1134. [[CrossRef](#)]

44. Shyn, T.W. Angular distribution of electrons elastically scattered from gases: 2–400 eV on He. *Phys. Rev. A* **1980**, *22*, 916. [[CrossRef](#)]
45. Puech, V.; Mizzi, S. Collision cross sections and transport parameters in neon and xenon. *J. Phys. D: Appl. Phys.* **1991**, *24*, 1974. [[CrossRef](#)]
46. Meunier, J.; Belenguer, P.; Boeuf, J.P. Numerical model of an ac plasma display panel cell in neon-xenon mixtures. *J. Appl. Phys.* **1995**, *78*, 1995. [[CrossRef](#)]
47. Robertson, A.G. The momentum transfer cross section for low energy electrons in neon. *J. Phys. B Atom. Mol. Phys.* **1972**, *5*, 648. [[CrossRef](#)]
48. Shi, X.; Burrow, P.D. Differential scattering cross sections of neon at low electron energies. *J. Phys. B At. Mol. Phys.* **1992**, *25*, 4273. [[CrossRef](#)]
49. Linert, I.; Mielewska, B.; King, G.C.; Zubek, M. Elastic electron scattering in neon in the 110°–180° scattering angle range. *Phys. Rev. A* **2006**, *74*, 042701. [[CrossRef](#)]
50. Cho, H.; McEachran, R.P.; Buckman, S.J.; Tanaka, H. Elastic electron scattering from neon at backward angles. *Phys. Rev. A* **2008**, *78*, 034702. [[CrossRef](#)]
51. Gulley, R.J.; Alle, D.T.; Brennan, M.J.; Brunger, M.J.; Buckman, S.J. Differential and total electron scattering from neon at low incident energies. *J. Phys. B At. Mol. Phys.* **1994**, **1994**, *27*, 2593. [[CrossRef](#)]
52. Kurokawa, M.; Kitajima, M.; Toyoshima, K.; Kishino, T.; Odagiri, T.; Kato, H.; Hoshino, M.; Tanaka, H.; Ito, K. High-resolution total-cross-section measurements for electron scattering from Ar, Kr, and Xe employing a threshold-photoelectron source. *Phys. Rev. A* **2011**, *84*, 062717. [[CrossRef](#)]
53. Hayashi, M. Bibliography of Electron and Photon Cross Sections with Atoms and Molecules Published in the 20th Century—Argon, Report. NIFS-DAT-72 of the National Institute for Fusion Science of Japan, Report NIFS-DATA-79; Japan National Institute for Fusion Science, Oroshicho, Toki, Gifu, Japan, 2003. Available online: <http://www.nifs.ac.jp/report/nifs-data072.html> (accessed on 1 August 2021).
54. Gibson, J.C.; Gulley, R.J.; Sullivan, J.P.; Buckman, S.J.; Chan, V.; Burrow, P.D. Elastic electron scattering from argon at low incident energies. *J. Phys. B* **1996**, *29*, 3177. [[CrossRef](#)]
55. Weyhreter, M.; Barzick, B.; Mann, A.; Linder, F. Measurements of differential cross sections for  $e$ -Ar, Kr, Xe scattering at  $E = 0.05 - 2$  eV. *Z. Phys. D* **1988**, *7*, 333. [[CrossRef](#)]
56. Cho, H.; Park, Y.S. Low-energy Electron Scattering from Argon. *J. Korean Phys. Soc.* **2009**, *55*, 459. [[CrossRef](#)]
57. Srivastava, S.K.; Tanaka, H.; Chutjian, A.; Trajmar, S. Elastic scattering of intermediate-energy electrons by Ar and Kr. *Phys. Rev. A* **1981**, *23*, 2156. [[CrossRef](#)]
58. Mielewska, B.; Linert, I.; King, G.C.; Zubek, M. Differential cross sections for elastic electron scattering in argon over the angular range 130°–180°. *Phys. Rev. A* **2004**, *69*, 062716. [[CrossRef](#)]
59. Buckman, S.J.; Lohmann, B. The total cross section for low-energy electron scattering from krypton. *J. Phys. B* **1987**, *20*, 5807. [[CrossRef](#)]
60. Ferch, J.; Simon, F.; Strakeljahn, G. Abstracts of Contributed Papers. In Proceedings of the 15th International Conference on the Physics of Electronic and Atomic Collisions, Brighton, UK, 22–28 July 1987; Geddes, J., Gilbody, H.B., Kingston, A.E., Latimer, C.J., Walters, H.J.R., Eds.; North-Holland: Amsterdam, The Netherlands, 1987; p. 132.
61. Jost, K.; Bisling, P.G.F.; Eschen, F.; Felsmann, M.; Walther, L. Abstracts of Contributed Papers. In Proceedings of the 13th International Conference on the Physics of Electronic and Atomic Collisions, Berlin, Germany, 27 July– 2 August 1983; Geddes, J., Gilbody, H.B., Kingston, A.E., Latimer, C.J., Walters, H.J.R., Eds.; North-Holland: Amsterdam, The Netherlands, 1983; p. 91.
62. Koizumi, T.; Shirakawa, E.; Ogawa, I. Momentum transfer cross sections for low-energy electrons in krypton and xenon from characteristic energies. *J. Phys. B* **1986**, *19*, 2331. [[CrossRef](#)]
63. England, J.P.; Eford, M.T. Momentum Transfer Cross Section for Electrons in Krypton Derived from Measurements of the Drift Velocity in H<sub>2</sub>-Kr Mixtures. *Aust. J. Phys.* **1988**, *41*, 701. [[CrossRef](#)]
64. Hunter, S.R.; Carter, J.G.; Christophorou, L.G. Low-energy electron drift and scattering in krypton and xenon. *Phys. Rev. A* **1988**, *38*, 5539. [[CrossRef](#)]
65. Mitroy, J. The Momentum Transfer Cross Section for Krypton. *Aust. J. Phys.* **1990**, *43*, 19. [[CrossRef](#)]
66. Pack, J.L.; Voshall, R.E.; Phelps, A.V.; Kline, L.E. Longitudinal electron diffusion coefficients in gases: Noble gases. *J. Appl. Phys.* **1992**, *71*, 5363. [[CrossRef](#)]
67. Brennan, M.J.; Ness, K.F. Momentum Transfer Cross Section for e-Kr Scattering. *Austr. J. Phys.* **1993**, *46*, 249. [[CrossRef](#)]
68. Zatsarinny, O.; Bartschat, K.; Allan, M. High-resolution experiments and B-spline R-matrix calculations for elastic electron scattering from krypton. *Phys. Rev. A* **2011**, *83*, 032713. [[CrossRef](#)]
69. Danjo, A. Electron scattering from Kr. I. Differential cross section for elastic scattering. *J. Phys. B* **1988**, *21*, 3759. [[CrossRef](#)]
70. Linert, I.; Mielewska, B.; King, G.C.; Zubek, M. Elastic electron scattering in krypton in the energy range from 5 to 10 eV. *Phys. Rev. A* **2010**, *81*, 012706. [[CrossRef](#)]
71. Cho, H.; Gulley, R.J.; Buckman, S.J. Elastic Electron Scattering from Krypton at Backward Angles. *J. Korean Phys. Soc.* **2003**, *42*, 71.
72. Alle, D.T.; Brennan, M.J.; Buckman, S.J. Abstract. In Proceedings of the 18th International Conference on Physics of Electronic and Atomic Collisions, Aarhus, Denmark, 21–27 July 1993; Andersen, T., Fastrup, B., Folkmann, F., Knudsen, H., Andersen, N., Eds.; American Institute of Physics: New York, NY, USA, 1993; p. 127.

73. Guskov, Y.; Savvov, R.V.; Slobodyanyuk, V.A. Time-of-flight measurements of the total cross-section for elastic scattering of low-energy electrons ( $E = 0.025\text{--}1.0$  eV) by He, Ne, Ar, Kr and Xe. *Sov. Phys. Tech. Phys.* **1978**, *23*, 167.
74. Schmidt, B.; Berkhan, K.; Götz, B.; Müller, M. New experimental techniques in the study of electron swarms in gases and their impact on the determination of low energy electron scattering cross sections. *Phys. Scr.* **1994**, *53*, 30. [[CrossRef](#)]
75. Hayashi, M. Bibliography of Electron and Photon Cross Sections with Atoms and Molecules Published in the 20th Century—Xenon. In *Research Report NIFS-DATA Series*; Report NIFS-DATA-79; Japan National Institute for Fusion Science: Toki, Japan, 2003.
76. Register, D.F.; Vuskovic, L.; Trajmar, S. Elastic electron scattering cross sections for Xe in the 1–100 eV impact energy region. *J. Phys. B At. Mol. Phys.* **1986**, *19*, 1685. [[CrossRef](#)]
77. Gibson, J.C.; Lun, D.R.; Allen, L.J.; McEachran, R.P.; Parcell, L.A.; Buckman, S.J. Low-energy electron scattering from xenon. *J. Phys. B At. Mol. Phys.* **1998**, *31*, 3949. [[CrossRef](#)]
78. Linert, I.; Mielewska, B.; King, G.C.; Zubek, M. Differential cross sections for elastic electron scattering in xenon in the energy range from 5 eV to 10 eV. *Phys. Rev. A* **2007**, *76*, 032715. [[CrossRef](#)]
79. Reisfeld, G.; Asaf, U. Relation between the electron scattering length and the van der Waals approximation to the equation of state. *Phys. Rev. A* **1994**, *49*, 348. [[CrossRef](#)]
80. Szymtkowski, R. Calculation of the electron-scattering lengths for rare-gas atoms. *Phys. Rev. A* **1995**, *51*, 853. [[CrossRef](#)]
81. Borghesani, A.F.; Santini, M.; Lamp, P. Excess electron mobility in high-density gas. *Phys. Rev. A* **1992**, *46*, 7902. [[CrossRef](#)]
82. Borghesani, A.F.; Santini, M. Electron localization-delocalization transition in high-density neon gas. *Phys. Rev. A* **1992**, *45*, 8803. [[CrossRef](#)]
83. Borghesani, A.F. Accurate Electron Drift Mobility Measurements in Moderately Dense Helium Gas at Several Temperatures. *Atoms* **2021**, *9*, 52. [[CrossRef](#)]
84. McEachran, R.P.; Stauffer, A.D. Polarisation and exchange effects on elastic scattering of electrons from helium. *J. Phys. B At. Mol. Phys.* **1983**, *16*, 255. [[CrossRef](#)]
85. Hudson, E.T.; Bartschat, K.; Scott, M.P.; Burke, P.G.; Burke, V.M. Electron scattering from helium atoms. Phase shifts, resonance parameters and total cross sections. *J. Phys. B At. Mol. Phys.* **1996**, *29*, 5513. [[CrossRef](#)]
86. Williams, J.F. A phaseshift analysis of experimental angular distributions of electrons elastically scattered from He, Ne and Ar over the range 0.5 to 20 eV. *J. Phys. B At. Mol. Phys.* **1979**, *12*, 265. [[CrossRef](#)]
87. Ferch, J.; Raith, W.; Schröder, K. Total cross section measurements for electron scattering from molecular hydrogen at very low energies. *J. Phys. B At. Mol. Phys.* **1980**, *13*, 1481. [[CrossRef](#)]
88. Garbaty, E.A.; LaBahn, R.W. Scattering of Slow Electrons by Neon and Argon. *Phys. Rev. A* **1971**, *4*, 1425. [[CrossRef](#)]
89. O'Malley, T.F.; Crompton, R.W. Electron-neon scattering length and S-wave phaseshifts from drift velocities. *J. Phys. B Atom. Mol. Phys.* **1980**, *13*, 3451. [[CrossRef](#)]
90. McEachran, R.P.; Stauffer, A.D. Elastic scattering of electrons from neon and argon. *J. Phys. B At. Mol. Phys.* **1983**, *16*, 4023. [[CrossRef](#)]
91. Dasgupta, A.; Bhatia, A.K. Scattering of electrons from neon atoms. *Phys. Rev. A* **1984**, *30*, 1241. [[CrossRef](#)]
92. Saha, H.P. Low-energy elastic scattering of electrons from neon atoms. *Phys. Rev. A* **1989**, *39*, 5048. [[CrossRef](#)] [[PubMed](#)]
93. Ferch, J.; Raith, W. University of Bielefeld, Germany, Unpublished work, 1985
94. Kumar, V.; Krishnakumar, E.; Subramanian, K.P. Electron-helium and electron-neon scattering cross sections at low electron energies using a photoelectron source. *J. Phys. B At. Mol. Phys.* **1987**, *20*, 2899. [[CrossRef](#)]
95. Guillemaut, C.; Pitts, R.A.; Kukushkin, A.S.; Gunn, J.P.; Bucalossi, J.; Arnoux, G.; Belo, P.; Brezinsek, S.; Brix, M.; Corrigan, G.; et al. Influence of atomic physics on EDGE2D-EIRENE simulations of JET divertor detachment with carbon and beryllium/tungsten plasma-facing components. *Nucl. Fusion* **2014**, *54*, 093012. [[CrossRef](#)]